JOURNAL OF CATALYSIS 150, 356–367 (1994)

Pd–Fe/SiO_2 Catalysts in the Hydrogenation of 2,4-Dinitrotoluene

F. Pinna,*,[1] M. Selva,* M. Signoretto,* G. Strukul,* F. Boccuzzi,†
A. Benedetti,‡ P. Canton,‡ and G. Fagherazzi‡

*Dipartimento di Chimica, Università di Venezia, Calle Larga St. Marta 2137, I-30123 Venezia, Italy; †Dipartimento di Chimica Inorganica, Chimica Fisica e Chimica dei Materiali, Università di Torino, I-10125, Torino, Italy; and ‡Dipartimento di Chimica Fisica, Università di Venezia, Calle Larga St. Marta 2137, I-30123 Venezia, Italy

Received January 21, 1994; revised July 5, 1994

Pd–Fe/SiO_2 bimetallic catalysts with a constant amount of Pd and a different Fe/Pd ratio were prepared by sequential wet impregnation and the hydrogenation of 2,4-dinitrotoluene was carried out at 25°C in a batch reactor. The presence of Fe enhances the Pd catalytic activity. The formation of a dispersed Pd–Fe alloy was evidenced through X-ray powder diffraction and is consistent with the data observed by FTIR analysis, TPR, and chemisorption features. The increase of the Fe total content of the catalysts results in the increase of the dispersion of the metallic phase and in the presence of partially oxidized Fe species. FTIR analysis shows that nitrocompounds chemisorb mainly on the support rather than on the metal surface. It is suggested that the Pd–Fe alloy formation is responsible for the increase of the catalytic activity because of a cooperative effect of Fe in the hydrogen transfer step. © 1994 Academic Press, Inc.

INTRODUCTION

Bimetallic catalysts are a topic of great interest in catalysis because of their industrial impact and their intrinsic scientific interest, since the performance of the bimetallic species often differs from that of their components. The first significant commercial application of bimetallic catalysts has been the use of Pt–Re (1) and Pt–Ir (2) systems in naphtha reforming and more recently NiCu (3) and NiCoCu (4) systems were applied to the hydrogenation of aromatics and high molecular weight olefins in the solvent industry.

Many papers have been published (5–7) on the selective hydrogenation of olefins, aromatics, and alkynes with bimetallic catalysts, in particular with combination of group VIII–IB metals. As a general result, it is observed that the interaction of group IB with group VIII metals reduces the self-poisoning of the catalyst during the reaction and the catalytic activity decreases with the increase of the IB concentration.

[1] To whom correspondence should be addressed. Fax: +39 41 5298517; e-mail: pinna@vega.cicsd.unive.it.

On the other hand little information is reported in the literature concerning the hydrogenation of nitroaromatic compounds to the corresponding amines, particularly for the hydrogenation of dinitrotoluene to toluenediamine with precious bi- or multimetallic catalysts. Mallat *et al.* found that Pd–Co/graphite (8) and Pt–Au (9) catalysts are more active in the hydrogenation of nitrobenzene than unalloyed Pd and Pt and recently Galvagno *et al.* (10) have shown that upon addition of tin, the catalytic activity of Pt increases at low tin content and then decreases at higher Sn/Pt ratios. According to this author, at low concentration tin ions could act as promoters in the activation of the nitro group. Two Du Pont patents (11, 12) claim an increase of the hydrogenation rate for aromatic nitrocompounds to form amines, by using iron-activated platinum or palladium catalysts supported on "highly oleophilic" carbon black. Strätz (13) described the influence of the preparation method and promoter metals on the activity of some palladium-based catalysts supported on carbon operating at 25°C and atmospheric pressure. The improvement of activity in coprecipitated Pd, Pt, and Fe was described as a typical example of synergistic effect.

In a previous work we reported on the effect of a second metal component like Cu, Sn, or Fe on the Pd/SiO_2 activity in the hydrogenation of 2,4-dinitrotoluene and we found that, unlike copper and tin, iron addition increased the catalytic activity of palladium (14).

The aim of the present work is to study in greater detail both the effect of iron on the hydrogenation activity of Pd/SiO_2 and the phase structure of the bimetallic catalysts. PdFe/SiO_2 samples were prepared by sequential impregnation and were characterized using the following techniques: temperature-programmed reduction (TPR), X-ray powder diffraction (XRPD), Fourier transform infrared spectroscopy (FTIR), CO, H_2, and O_2 chemisorption, and high-resolution transmission electron microscopy (HRTEM). The catalytic hydrogenation of 2,4-dinitrotoluene was studied in a batch slurry reactor.

0021-9517/94 $6.00

TABLE 1

Analytical Data of the Catalysts

No.	Catalyst	Pd (wt%)	Fe (wt%)	Fe/Pd (atomic)
1	Pd	2.19	—	0.0
2	Pd–Fe	2.11	0.54	0.49
3	Pd–Fe	2.02	0.77	0.73
4	Pd–Fe	1.95	0.99	0.97
5	Pd–Fe	2.06	1.68	1.55
6	Pd–Fe	1.99	2.23	2.13
7	Pd–Fe	2.04	4.47	4.17
8	Fe	—	2.01	—

EXPERIMENTAL

Catalyst Preparation

Catalysts were prepared by sequential wet impregnation of SiO_2 (Akzo Chemie F22; surface area 400 $m^2\ g^{-1}$; particle size range: 100–150 μm) with $PdCl_2$ and $FeCl_3$ solutions. $PdCl_2$ was dissolved with HCl (0.2 *M*) and the H_2PdCl_4 that formed was slowly added to the support, which was then left under stirring for 18 h. The excess of water was removed by slow evaporation in rotavapor. After drying at 110°C for 4 h, different batches of the same sample were impregnated with aqueous solutions of $FeCl_3$ with the same procedure, in order to obtain the bimetallic catalysts with different Fe/Pd ratios. After drying, the samples were calcined at 550°C for 2 h, reduced in H_2 flow at 250°C for 1 h, and passivated (5% O_2 in Ar) before storing in air.

Two monometallic Pd/SiO_2 and Fe/SiO_2 were prepared with the same procedure.

The chemical analysis of the two metals was performed by atomic absorption spectroscopy. The results are reported in Table 1.

Catalyst Characterization

Temperature-programmed reduction measurements were performed in a previously described standard apparatus (15). The calcined samples (500°C) were heated at a linear rate of 15°C/min from 25 to 800°C with a gas (5% H_2 in Ar) mixture (40 ml at STP/min). The H_2 consumption was calculated by integration of the TPR profiles and calibrated both by reduction of known amounts of CuO and by injecting known amounts of H_2.

X-ray powder diffraction patterns were collected using a Philips vertical goniometer connected to a highly stabilized generator. Cu$K\alpha$ radiation, a graphite monochromator and a proportional counter with pulse-height discrimination were used. A step-by-step technique was employed with steps of 0.05° in 2θ and an accumulation counting time of 100 s per angular abscissa. All irradiated powder samples, contained in geometrically equal holders, had the same weight and were uniformly prepared. In order to separate the decreasing background scattering, due to the support, from the Bragg peaks of the crystalline phases, a profile-fitting procedure was used, in the investigated angular range of 30–50°, as described elsewhere (16). Due to the relevant broadening and weakness of the XRPD peaks of the active metal phase, only the line broadening (LB) of the most intense 111 reflection could be measured. From the so-obtained optimized parameters of the best-fitted pseudo-Voigt functions describing the $K_{\alpha 1}$–$K_{\alpha 2}$ components of this reflection, a single-peak Fourier analysis was straightforwardly performed by attributing the observed LB to crystallite size effects only (after having eliminated the instrumental LB) (16, 17). In such a way a volume-weighted crystallite size, $\langle D\rangle_v$, as measured perpendicularly to the (111) lattice planes, was obtained. This procedure is equivalent to employing the Scherrer equation starting from the integral breadth, but, with the Fourier analysis, the instrumental broadening can be deconvoluted with higher accuracy.

The unit cell edge of the palladium-based fcc structure could be obtained with good accuracy from the peak maximum best-fitted angular position, PPM (estimated error $\pm 0.02°$ in 2θ). In order to determine the possible presence of lattice microstrain, the single-peak method of Nandi *et al.* (18) was computerized and employed starting from the $A(L)$ Fourier transform of the "true" $K_{\alpha 1}$ analytically expressed peak profile, where L is the variable in the real space. A surface-weighted average crystallite size could be computed from the intercept on the L axis of the initial slope of the $A(L)$ vs L function. The lower the microstrain, the better these values may be estimated. The method of Nandi *et al.* makes the approximation

$$\lim_{L\to 0} A(L) \approx 1 - L/M,$$

where $(3/2)M$ is a surface-weighted spherically averaged particle size. Bearing in mind that $A(L) = A^S(L)A^D(L)$ and approximating the size component $A^S(L)$ of the Fourier transform $A(L)$ to the exponential expression $\exp(-L/M)$, the lattice disorder component $A^D(M/2)$ may be calculated on the basis of the fundamental Warren–Averbach equation (19). From the $A^D(M/2)$ value the rms microstrain $\langle\varepsilon^2\rangle^{1/2}$ at $M/2$ may be immediately obtained.

H_2, O_2, and CO chemisorption and O_2–H_2 titration measurements were performed using a pulse flow technique (15). Prior to measurement, each sample was subjected to a thermal pretreatment which involved exposure to H_2 at 250°C for 2 h followed by Ar purge at the same

temperature for 3 h. The samples were then cooled in Ar flow to 25°C for measurement of CO and O_2 chemisorption and to 70°C for H_2 chemisorption to avoid β-hydride formation with Pd (20). The titration of O_2 chemisorbed at 25°C was performed with H_2 at 90°C.

HRTEM micrographs were made with a JEOL 2000 EX electron microscope, equipped with a top entry stage. The powder was ultrasonically dispersed in isopropyl alcohol and the suspension was deposited on a copper grid coated with a holey carbon film.

Fourier transform infrared spectra were recorded with a 1760 Perkin–Elmer FTIR spectrometer at 25°C. The powders were pressed in pellets and submitted, in the IR cell, to different thermal and chemical treatments.

Catalytic Activity

The hydrogenation of 2,4-dinitrotoluene was carried out in ethanol solution at atmospheric pressure in a 25-ml round-bottomed flask equipped with a hydrogen reservoir (10 liters) and a side arm fitted with a screw-capped silicone septum to allow sampling. Constant temperature (25 ± 0.5°C) was maintained by water circulation in an external jacket connected with a thermostat. Stirring was performed by a teflon-coated bar driven externally by a magnetic stirrer. Absence of diffusional problems was determined by the independence of conversion vs time plots on the stirring rate in kinetic experiments.

The catalyst (40 mg) was placed in the reactor, which was evacuated and filled with H_2. Then 10 ml of a H_2-saturated, 0.2 *M* solution of DNT in ethanol, containing *n*-decanol (0.05 *M*) as internal standard, was added through the septum and time was started. All reactions were monitored with GLC by direct injection of samples taken periodically from the reaction mixtures with a micro syringe. Separation of the products was performed on a 2-m OV17 packed column using a flame ionization detector. Quantitative data were obtained from calibration curves of the reactant and products vs the internal standard.

RESULTS AND DISCUSSION

TPR

The TPR profiles of the Pd–Fe catalysts after calcination at 500°C are shown in Fig. 1 together with Pd/SiO_2 and Fe/SiO_2 samples. The profile of the monometallic Pd catalyst (curve 1) shows a negative peak centered at about 80°C, indicating a hydrogen evolution, which has been attributed to the Pd β-hydride decomposition (21). The latter is formed because of H_2 absorption during the palladium reduction which takes places at $T < 0$°C (22, 23). The reduction profile of the Fe/SiO_2 sample (curve 8) shows a broad band with two maxima centered at about

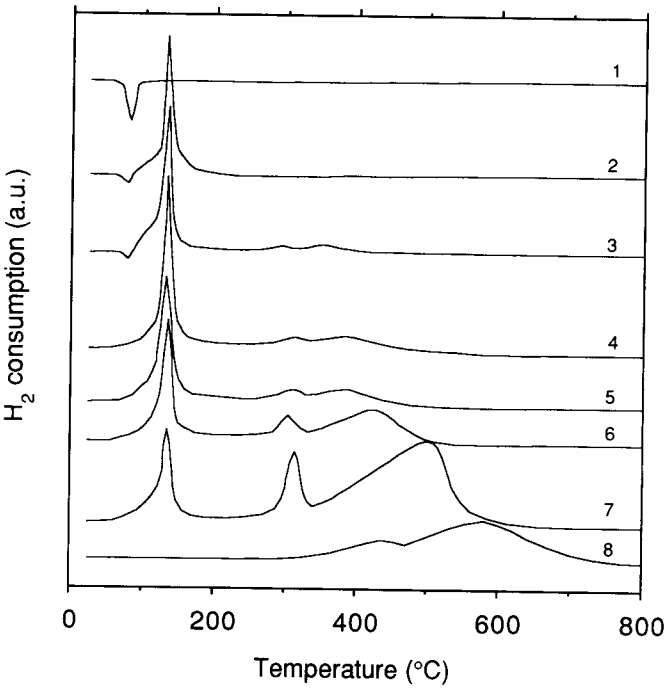

FIG. 1. TPR profiles of the individual samples calcined at 550°C. Numbering on curves refer to sample numbering reported in Table 1. With reference to the peak centered at $T = 135$°C, the following H_2/Pd values are calculated: sample 2, 0.8; sample 3, 1.0; sample 4, 1.4; sample 5, 1.3; sample 6, 1.1; sample 7, 1.2.

440 and 590°C, which have been attributed (24) to a two-stage reduction of Fe_2O_3 to Fe^0 through Fe_3O_4.

In all the profiles of the bimetallic samples (curves 2–7), a new sharp peak appears at about 135°C, while the negative peak at about 80°C is still present in samples 2 and 3 (curves 2 and 3), its intensity decreasing with the increase of the Fe content. The reduction band of Fe_2O_3 shifts to lower temperatures and becomes smaller with the decrease of the Fe/Pd atomic ratio, eventually disappearing in curve 2.

All these findings suggest the occurrence of a strong interaction between Pd and Fe that, on the one hand, hinders the reduction of PdO at low temperature and, on the other, favours the reduction of Fe_2O_3.

Interaction of reduced Pd particles with iron cations and, under special conditions, alloy formation in Pd–Fe catalysts have been reported in the literature (21, 25–27). Moreover, it has been shown that the presence of a noble metal, like Pt or Pd, enhances significantly the reducibility of iron (28–30). In particular, by a comparison of TPR and Mössbauer measurements, Lietz *et al.* (21) have shown the formation of an intermetallic compound, called disordered alloy of composition Pd_xFe ($2 < x < 3$), which has been related to a TPR reduction peak centered at about 100°C. Furthermore, the composition of the alloy

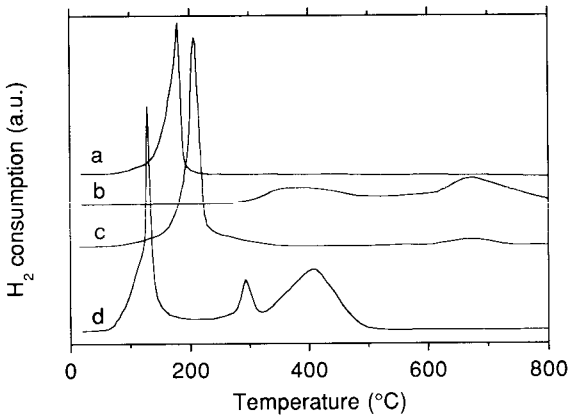

FIG. 2. TPR profiles of different salts impregnated on SiO_2 and dried at 110°C: (a) H_2PdCl_4; (b) $FeCl_3$; (c) H_2PdCl_4 + $FeCl_3$; (d) sample 6 of Table 1.

appeared to be relatively independent of the elemental composition of the samples.

In order to assign the peak at 135°C present in all the profiles of the bimetallic catalysts (Fig. 1), additional TPR measurements have been performed on samples, prepared by impregnation and subsequent drying at 110°C, of (i) H_2PdCl_4, (ii) $FeCl_3$, and (iii) H_2PdCl_4 + $FeCl_3$, all on SiO_2. The experimental results are shown in Fig. 2. This also includes the Pd–Fe sample 6 (curve d) of Fig. 1 for comparison.

The profile a, relative to H_2PdCl_4/SiO_2, shows a peak at about 185°C which can be ascribed to the reduction of a palladium chloride or a palladium oxychloride species stabilized on the support and formed after drying at 110°C, as already suggested for Pd/Al_2O_3 catalysts (23). Similarly, in the TPR of H_2PdCl_4 + $FeCl_3/SiO_2$ (curve c), the peak at about 215°C can be ascribed to the reduction of a mixed Pd and Fe oxy/hydroxychloride species stabilized on the support. The small band which appears at $T >$ 650°C is probably due to the reduction of a little F_2O_3 already formed, by comparison with the profile of $FeCl_3/SiO_2$ (curve b). In the latter, the band in the range 350–480°C can be ascribed to the reduction of a hydroxychloride and/or a hydroxyl species of iron (31) formed after drying at 110°C. It is worth noting that the TPR spectra of the H_2PdCl_4 + $FeCl_3/SiO_2$ sample (curve c), after calcining at 500°C becomes almost identical to the profile of the bimetallic catalysts (curve d).

Going back to the H_2 consumption relative to the peak at T = 135°C in Fig. 1, it appears that the ratio H_2/Pd increases with the amount of iron up to a maximum for sample Pd–Fe 4 and then decreases for higher contents of iron. It is interesting to note that, in most cases (samples 4–7), the H_2/Pd values exceed unity, suggesting that the peak at T = 135°C has to be associated not only to the reduction of the PdO species, but also to the reduction of some Fe_2O_3 with the formation of a Pd–Fe intermetallic compound. On the other hand, given the uncertainty concerning the complete reduction of Pd in the catalysts, as indicated by the H_2/Pd ratio $\leq$ 1 for samples 2, 3, a quantitative evaluation of the relative amounts of Pd and Fe associated with the intermetallic compound on the basis of the TPR data is not possible.

X-ray Powder Diffraction

The X-ray powder diffraction patterns of the Pd–Fe samples 2–6 are shown in Fig. 3, where the XRPD pattern of the monometallic Pd sample 1 is also recorded for comparison. As can be seen, the position and the area of the 111 palladium profile are influenced by the addition of the second metal. The PPM best-fitting analysis showed that in all Pd–Fe catalysts this peak, when present, shifts by about the same $\Delta 2\theta$ displacement (about +0.2°), with respect to Pd/SiO_2 (see, for example, Fig. 4, where the best-fitting results for samples 1 and 2 are shown). In our opinion this suggests the formation of an alloy in the bimetallic catalysts. Bearing in mind that the edge of the fcc unit cell of Pd_3Fe is 0.3851 nm (32) and the edge of the fcc unit cell of dispersed pure palladium is 0.3890 nm (16), this systematic displacement can be explained as the result of formation of a Pd_xFe_{1-x} alloy with x = 0.87 ± 0.03, assuming a linear decrease in the unit cell edge with the increase in the iron content.

For the same samples, Table 2 shows the volume-weighted $\langle D \rangle_v$ crystallite size as well as the surface-weighted average crystallite size (assumed to be of spherical shape), $(3/2)M$, as determined with Nandi's procedure. The $\langle \varepsilon^2 \rangle^{1/2}$ values determined by this procedure are also reported in Table 2. The two series of

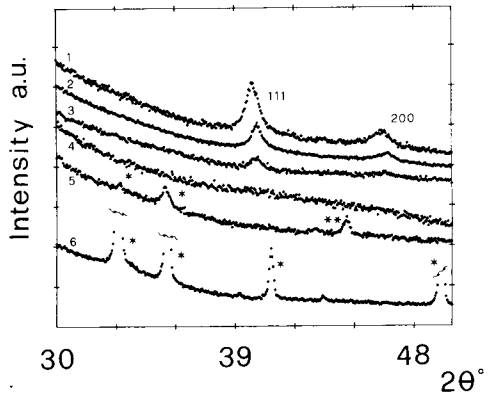

FIG. 3. XRPD patterns of the individual samples after reduction at 250°C. Numbering on curves refer to sample numbering reported in Table 1. The 111 and 200 peaks of the fcc crystal structure (Pd or Pd–Fe alloy) are shown. An asterisk indicates α-Fe_2O_3 peaks, whereas a double asterisk indicates α-Fe peak.

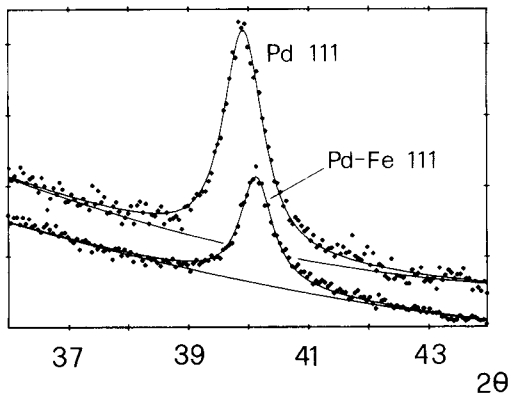

FIG. 4. The angular shift toward higher Bragg angles present in the XRPD of bimetallic catalysts (sample 2 in this case) as shown by profile best-fitting procedures.

TABLE 3

Chemisorption Data after H_2 Reduction at 250°C

No.	Catalyst	Fe/Pd	H_s/Pd	O_s/Pd	H_T/Pd	H_T/O_s	CO/Pd
1	Pd	0.0	0.23	0.25	0.70	2.8	0.20
2	Pd–Fe	0.49	0.13	0.29	0.63	2.2	0.17
3	Pd–Fe	0.73	0.14	0.35	0.66	1.9	0.12
4	Pd–Fe	0.97	0.16	0.39	0.72	1.8	0.20
5	Pd–Fe	1.55	0.24	0.54	0.88	1.6	0.18
6	Pd–Fe	2.13	0.26	0.63	1.06	1.7	0.15
7	Pd–Fe	4.17	0.31	0.85	1.32	1.5	0.13

Note. H_s/Pd, O_s/Pd, and CO/Pd are respectively the number of hydrogen and oxygen atoms and carbon monoxide molecules chemisorbed per Pd atom in the sample; H_T/Pd is the number of hydrogen atoms titrating the oxygen chemisorbed per Pd atom in the sample.

size values are close to one another and show that, up to an iron content of 0.77 wt%, the crystallite sizes corresponding to 111 XRPD peaks are fairly similar for all catalysts. On the other hand, by increasing the iron content up to 0.99 wt% (patterns 1–4 of Fig. 3) a systematic decrease of the peak areas is clearly evident. In particular, in pattern 4 (0.99 wt% of Fe), all XRPD peaks disappear. This can indicate that more and more crystallites, in the metallic phase, fall below the size limit of XRPD detectability (≤1.5–2.0 nm) with a consequent increase of dispersion and/or that the lattice order and the cristallinity of the metallic phase decrease in this composition range. Fluctuations in the local composition can also reduce the XRPD detectability of the metallic phase.

In samples containing more than about 1 wt% Fe (patterns 5 and 6 of Fig. 3), α-Fe_2O_3, either alone or together with α-Fe, begins to appear, while the alloy remains undetectable.

By means of various structural techniques (especially Mössbauer spectroscopy) several authors (21, 25, 33, 34) found in Pd–Fe bimetallic supported catalysts the formation of Pd_xFe_{1-x} alloys having different compositions. In particular, in the paper by Lietz *et al.* (21) the composition of the Pd_xFe_{1-x} alloys on silica was estimated in the range $0.67 < x < 0.80$ for catalysts containing about 2 wt% of Pd, as in our case. The value of $x = 0.87$ found in our analysis approaches the upper limit found by Lietz *et al.* in catalysts reduced at higher temperatures.

In accordance with similar results reported elsewhere (21, 33), over a limiting quantity of iron, the effect of palladium in promoting the reduction of iron appears to be significantly diminished. The fact that α-Fe XRPD peaks sometimes appear in catalysts with a relatively high iron content is probably due to the presence of large particles, the cores of which were not completely oxidized during the passivation process. In the paper by Lietz *et al.* (21), in which Mössbauer measurements were taken under hydrogen atmosphere, separate particles of α-Fe appeared at an iron content of about 3 wt%.

TABLE 2

Microstructural Parameters Determined by XRPD on the Metal Phase of the Catalysts with Higher Particle Size

Sample no.	Angular shift $\Delta 2\theta^\circ_{111}$	Crystallite size (nm)		Microstrain $\langle \varepsilon^2 \rangle^{1/2}_{M/2} (\times 10^4)$
		(3/2)M	$\langle D \rangle_v$	
1	—	6.6	6.8	8
2	+0.20 ± 0.02	6.4	5.7	9
3	+0.16 ± 0.02	7.2	7.4	7

Chemisorption Measurements

In Table 3 the chemisorption data of H_2, O_2, CO, and H_2/O_2 titration are reported. While a good consistency can be observed for the Pd/SiO_2 samples, the results for the bimetallic catalysts should be, in principle, taken only in a qualitative sense because the stoichiometries of chemisorption are unknown and therefore the metallic dispersion and the mean particle size cannot be calculated. However, some interesting observations can be made by comparing the monometallic catalyst with the bimetallic ones.

The O_2 chemisorption for the Pd–Fe catalysts is always above that of pure Pd and increases with the amount of Fe. CO and H_s values for the Pd–Fe catalysts are initially below those of pure Pd; for Pd/Fe ratios > 1 the two sets of chemisorption data slightly diverge: CO smoothly decreases, while H_s shows an increasing trend in the whole range investigated.

If we now assume that the stoichiometries of H_S and CO adsorption on Pd surface sites do not change significantly with the addition of Fe, the observed decrease in the amount of CO and H_s chemisorbed on the samples with Fe/Pd ratios <1 indicates that in this composition range, the exposed Pd surface sites decrease with respect to Pd alone. This finding is also confirmed by FTIR data that will be discussed later on.

Since in all the examined samples Pd content is practically constant, the O_s chemisorption values seem to suggest the formation of reduced Fe sites capable of chemisorbing increasing amounts of O_2. Furthermore, this oxidized Fe sites can be rereduced in H_2 at 70°C as shown by the results (H_T/Pd) of the titration with H_2 of the previously chemisorbed O_2. This behaviour is similar to that previously reported in the literature for PtFe/C (35) and PdFe/η–Al_2O_3 catalysts (26). According to these authors the reversible oxidation reduction of Fe is a convincing evidence of bimetallic cluster formation.

Further information on the surface composition of the catalysts comes from the H_T/O_s data reported in Table 3. These clearly indicate that the reversible oxidation-reduction capacity of the catalyst surface decreases with the iron content. This observation may be indicative either of the formation of alloys of different composition, or of a decoration of the metal surface with increasing amount of iron species (see, below, the FTIR experiments) that are easy to oxidize, but more difficult to reduce, or, more likely, of the occurrence of both phenomena at the same time.

HRTEM

The bimetallic samples and, as a reference, the monometallic Pd/SiO_2 and Fe/SiO_2, reduced in H_2 at 250°C, were examined by HRTEM at different magnifications. Pd/SiO_2 micrographs show metallic particles of different, irregular shapes and sizes in the range 3–30 nm, while the Fe/SiO_2 micrographs show no metallic particles. As for the bimetallic samples, strong differences were observed in the metal particle size, between the samples with an Fe/Pd < 1 and those with an Fe/Pd > 1. In samples with a low iron loading, metallic particles of sizes similar to that of the pure Pd sample were observed, while in samples with a high iron content only metallic particles of size lower than 3 nm were detected. Figures 5a and 5b show photomicrographs at two different magnifications of sample 3; Figs. 5c and 5d show sample 5 at the same magnifications. The shown micrographs are quite typical and representative; it can be observed that the metallic particles shown in Fig. 5b display a highly disordered microstructure; in fact polycrystalline aggregates, stacks, and dislocations are detected and composition fluctuations can be suspected on the basis of parallel fringes irregularly spaced.

FTIR

Figure 6 shows the spectra, normalized to the same Pd content, obtained after interaction with 20 Torr of CO on samples 3–6, reduced under H_2 at 250°C; as a reference, the spectra of CO adsorbed on Pd/SiO_2 (sample 1) and on Fe/SiO_2 (sample 8), pretreated in the same way, are also shown.

On the Pd/SiO_2 sample (Fig. 6, curve 1) the CO interaction produces two absorptions; the first one, at 2088 cm^{-1}, is assigned to CO linearly chemisorbed on Pd surface sites, and the second one shows a maximum at 1945 cm^{-1} and a shoulder at 1988 cm^{-1}, assigned to bridge bonded CO in two different surface configurations (36). It is well known that on pure Pd monocrystalline surface, the CO is adsorbed mainly in the bridged form, while on Pd small particles a larger intensity of linearly adsorbed CO is observed, as a consequence of the fact that on these samples a relevant fraction of metallic surface atoms are borderline. In our sample the ratio between bridge and linearly bonded CO, in agreement with literature data on similar samples (37), suggests a dispersion of the metallic particles consistent with the chemisorption, HRTEM, and XRPD data.

For a more precise assignment of the observed bands, it can be recalled that on monocrystalline Pd (100) face, at full coverage, a band at 1983 cm^{-1} was observed (36), while on Pd (111) plane under similar conditions bands at 1946 and 2092 cm^{-1} were reported (36). Therefore, on this basis, we can assign the observed bands to CO chemisorbed on different surface planes, (100) and (111) exposed by the small particles.

On Fe/SiO_2 (Fig. 6, curve 5) the CO interaction does not produce any absorption band. This finding is in agreement with the TPR results, where no reduction was observed at temperatures lower than 400°C and IR literature data (38) showing that CO is not adsorbed on oxidized iron.

As for the bimetallic samples we observe that, in spite of the fact that all the samples have the same Pd content, significant differences are observed in (i) the total integrated intensity of the bands, (ii) the ratio between the different components, and (iii) the frequency of the observed maxima. The Pd–Fe sample 3 (Fig. 6, curve 2) shows bands in the same spectral region of Pd/SiO_2; however, the total area of the bands of this sample is significantly lower and the bridge to linear intensity ratio is considerably decreased. Moreover, the almost complete depletion of the shoulder at 1980 cm^{-1} is evident. At the same time, a small red shift of the linearly bonded CO from 2088 to 2084 cm^{-1}, and a broader shape of the band and a red shift of the bridge bonded CO from 1945 to 1928 cm^{-1} are also observed.

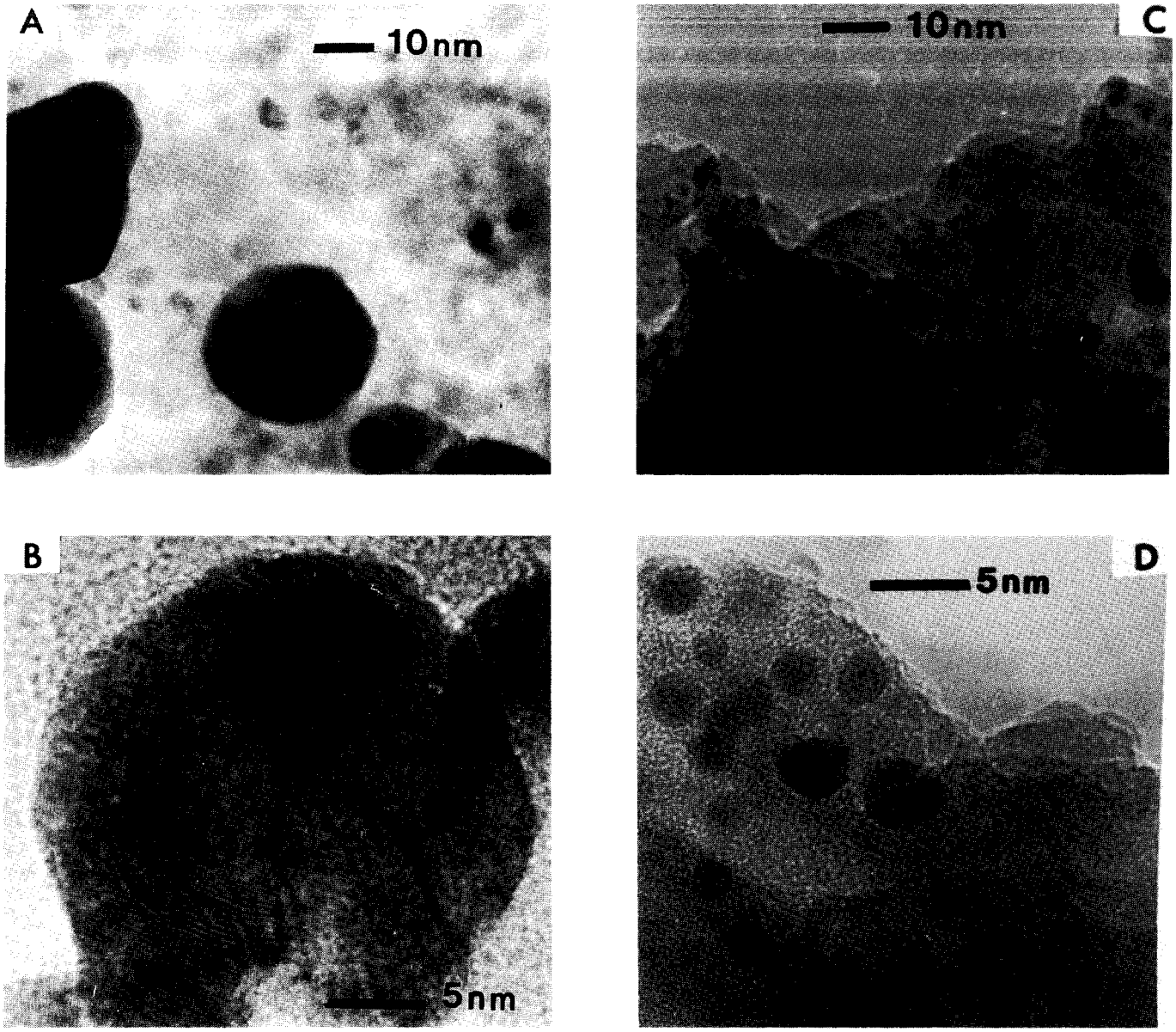

FIG. 5. Electron micrographs at two different magnifications of two Pd–Fe/SiO_2 samples: sections (A) and (B), sample 3; sections (C) and (D), sample 5. Section (B) shows a large polydomain particle composed by some coherent diffraction domains, the sites of which appear to be similar to those reported in Table 2, as determined by XRPD.

The almost complete depletion of the shoulder at 1980 cm^{-1} can be an indication that iron atoms or ions preferentially fill either the (100) sites or, more generally, the sites on which "compressed" bridged species can be formed. It can be recalled that on other bimetallic Pd-based systems (39) this phenomenon was not observed. As for the red shifts of the bands assigned to the linear and bridge bonded CO on (111) sites, these can be interpreted as due to a dilution effect caused by iron atoms or ions on the CO adsorbed on this surface plane. The dilution with atoms or ions not capable of chemisorbing CO produces a reduced chemical and dipole–dipole interaction between the adsorbed molecules. Since both chemical and dipole–dipole interactions on Pd surfaces normally cause a blue shift of the ν_{CO} stretching frequency (36), the dilution can explain an opposite shift.

The strong decrease in the CO absorption band of sample 3 with respect to those observed in sample 1 is a strong indication that the exposed Pd sites are strongly diminished, although XRPD data suggest that the average size of the metal particles remains almost constant in these samples. On the other hand, the bulk composition

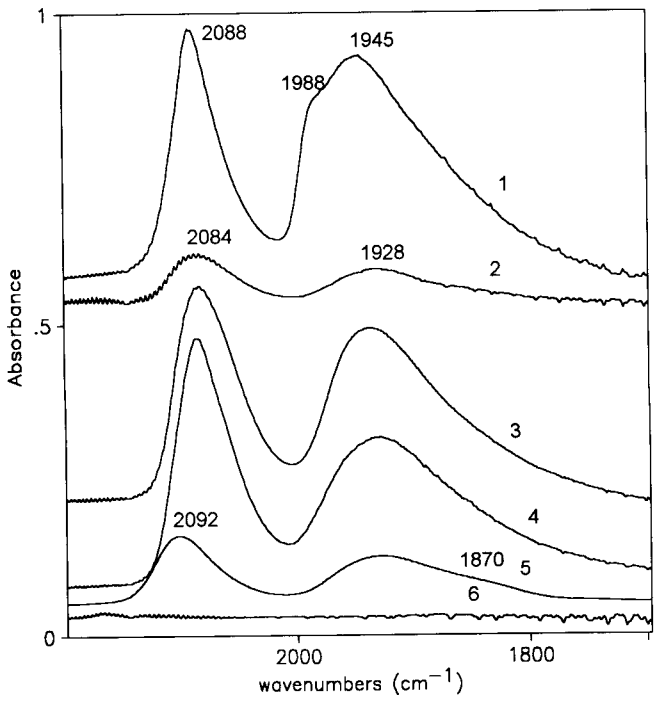

FIG. 6. Absorbance IR spectra of CO (20 Torr) adsorbed at room temperature on different samples: curve 1, sample 1; curve 2, sample 3; curve 3, sample 4; curve 4, sample 5; curve 5, sample 6; curve 6, Fe/SiO_2.

of the metal particles determined by XRPD is $Pd_{0.87}Fe_{0.13}$. On this basis an intensity reduction lower than 20% can be expected. However, strong differences between the bulk and the surface composition of bimetallic catalysts depending on the nature of the two alloyed elements and the composition of the surrounding atmosphere are reported in the literature (40). Therefore, the strong intensity reduction and the other spectroscopic features illustrated above can be interpreted only as a dilution and/or a decoration effect by iron species on the surface of the metallic particles.

On samples 4 and 5, CO interaction produces bands quite similar to those previously illustrated; however, the integrated intensities of the bands are appreciably different than in sample 3, in particular the total area is significantly larger. The increase of the total area of the bands of the chemisorbed CO on Pd sites on samples with a higher Fe content can be related to the XRPD and HRTEM data previously discussed, clearly revealing that the metallic dispersion of samples 4 and 5 is higher than that of sample 3. Sample 6 shows similar spectroscopic features; in addition a shoulder at 1870 cm^{-1} and the decrease in the intensity of the bands can be noted.

These observations confirm that in the bimetallic samples an interaction between the two metallic elements occurs, consistent with the formation of an alloy. In fact, in all bimetallic samples the Pd sites are less mutually interacting and more isolated, as a consequence of the presence of iron atoms, reducing the number of vicinal surface Pd sites, as shown by the lower ratio between the bridged and linearly bonded species and by the red shift of the bands.

However, these are only indirect evidences of the presence of iron on the metallic particles since CO chemisorption does not give indications on the nature of the surface iron species that modify the chemisorption and the catalytic properties of Pd in the bimetallic samples. NO is a more suitable test molecule for iron sites.

Figure 7 shows the IR absorption spectra produced by NO adsorption on samples 3, 5, and 6 (curves 3, 4, and 5 respectively); as references, in the same figure the spectra of NO adsorbed on Fe/SiO_2 and Pd/SiO_2 reduced at the same temperature (curves 1 and 2, respectively) and the spectrum of NO adsorbed on Fe/SiO_2 reduced at 400°C (curve 6) are reported. It is immediately evident that the spectra of NO chemisorbed on the bimetallic samples reduced at 25°C are very similar to that of the Fe/SiO_2 sample reduced at 400°C, while, with respect to the two monometallic samples reduced at 250°C, significant differ-

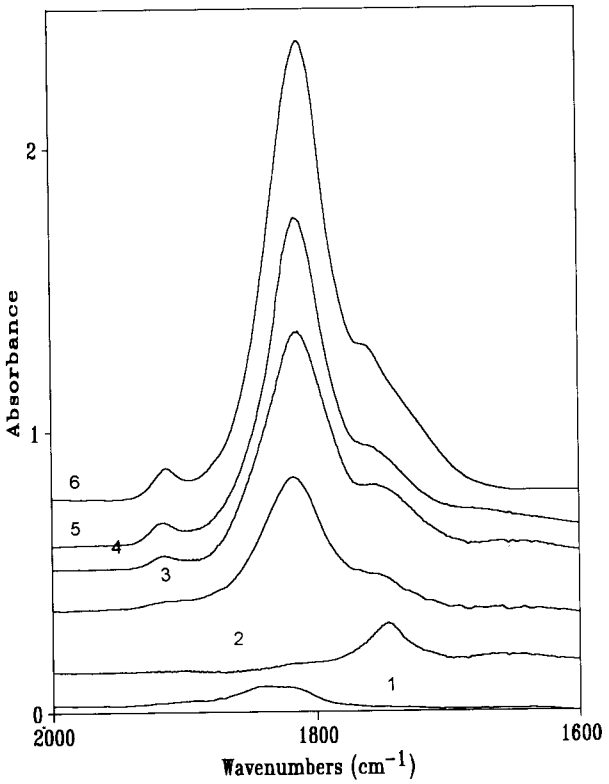

FIG. 7. Absorbance IR spectra of NO (10 Torr) adsorbed at room temperature on different samples: curve 1, Fe/SiO_2 reduced at 250°C; curve 2, sample 1; curve 3, sample 3; curve 4, sample 5; curve 5, sample 6; curve 6, Fe/SiO_2 reduced at 400°C.

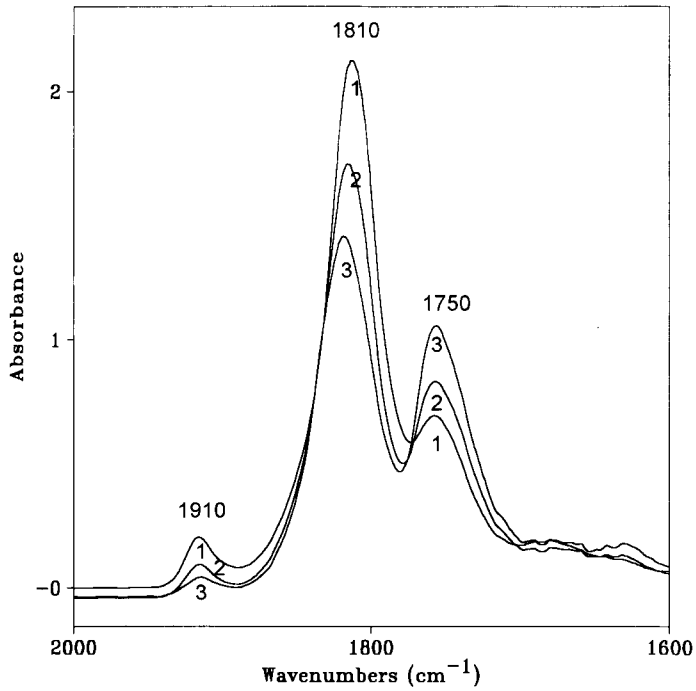

FIG. 8. Absorbance IR spectra of NO adsorbed on sample 4 at different coverages: curve 1, 10 Torr of NO; curve 2, 0.1 Torr of NO; curve 3, sample outgassed for 5 min.

ences are observed in the overall shape of the absorptions, their intensity, and the number and the frequency of the bands.

Figure 8 shows the spectra of NO adsorbed on sample 4 at full coverage (curve 1), after reduction of the equilibrium pressure (curve 2) and after outgassing (curve 3). Upon lowering the equilibrium pressure and upon evacuation the intensities of the bands at 1910 and 1810 cm^{-1} decrease and the band at 1750 cm^{-1} increases. These changes are similar to those described by Yuen *et al.* (41) in silica-supported iron samples. These authors assigned the bands at 1910 and 1810 cm^{-1} to the asymmetric and symmetric stretching of a Fe^{2+} dinitrosyl species and the bands at 1830 and 1750 cm^{-1} to the stretching of two different mononitrosyl species, on more coordinated and less coordinated Fe^{2+} ions, respectively. In our case the band at 1750 cm^{-1} could also be associated to a Pd^0 nitrosylic species. The presence of an isosbestic point between the bands at 1810 and 1750 cm^{-1} confirms that, as suggested by Yuen *et al.* (41), a conversion from a dinitrosylic to a mononitrosylic species occurs during the outgassing. The dinitrosylic species, particularly well defined on sample 4, the bimetallic sample showing the highest catalytic activity and in which all XRPD peaks are absent, is an indication that on this sample significant amounts of reduced, highly coordinatively unsaturated Fe^{2+} ions are present.

The iron(II) detected in FTIR NO adsorption experiments can be related to one of the following: (i) an incomplete iron reduction due to the mild reduction conditions of our experiments; (ii) the surface contamination of the bimetallic particles as a consequence of an incomplete removal of atmospheric oxygen; (iii) the dissociation of NO on Fe^0 sites exposed at the surface of the bimetallic particles leading to Fe^{II} formation.

Incompletely reduced iron species could be present as iron(II) silicate in agreement with proposal of Wielers *et al.* (31). According to these authors, silica, in the presence of water, either present on the surface or produced during the reduction process, becomes mobile and gives rise to an encapsulating layer of iron(II) silicate. In the second hypothesis, the reduction of the bimetallic samples leads to the formation of alloyed metallic particles, where the surface iron is present in a partially oxidized state, also after reductive and vacuum treatments, as a consequence of the high affinity of this element towards oxygen. This kind of behaviour has already been shown for other alloys containing oxophilic elements; for instance, it was demonstrated by XPS (42) that in a Ti–Cu alloy, prepared *in situ* under high vacuum conditions, a TiO_x layer covers the surface region. The third hypothesis, proposing that Fe^{II} sites are produced by dissociation of the test NO molecule, appears to be supported by the observation that NO absorption bands grow significantly with the contact time. The heat produced in the reaction can allow some atomic mobility, leading to an enrichment of iron on top of the metal particles, producing a "chemisorption induced surface segregation" of iron. Spectroscopic results of readsorption of CO after NO interaction (not reported here) confirm the latter hypothesis.

To investigate the nature of the active sites for the nitrogroup chemisorption and activation we have studied, by FTIR, the adsorption and hydrogenation of nitrobenzene on Pd–Fe samples 3, 5, and 6 and also, as references, on Pd/SiO_2 and on Fe/SiO_2. On all samples, nitrobenzene chemisorption produces strong bands at 1525 and 1354 cm^{-1}, assigned to the ν_a and ν_s of the NO_2 group and bands at 1606, 1580, and 1480 cm^{-1}, due to the ring vibrations. Moreover, bands are also observed in the C–H stretching region of aromatic compounds. As an example, in Fig. 9, curve 1, the spectrum produced by the adsorption on sample 3 is shown. The observed spectrum is remarkably similar to that recently reported by Koutstaal *et al.* (43) for the adsorption of nitrobenzene on pure silica. Moreover, we do not observe any difference in the chemisorbed species among the samples examined. On this basis, we suggest that the organic molecule is mainly adsorbed at the surface of the support.

By interaction with hydrogen, in all samples except Fe/SiO_2, the bands of nitrobenzene are depleted, while at the same time well defined bands at 1607 and 1500 cm^{-1}, easily assigned to aniline (44), are observed. Moreover,

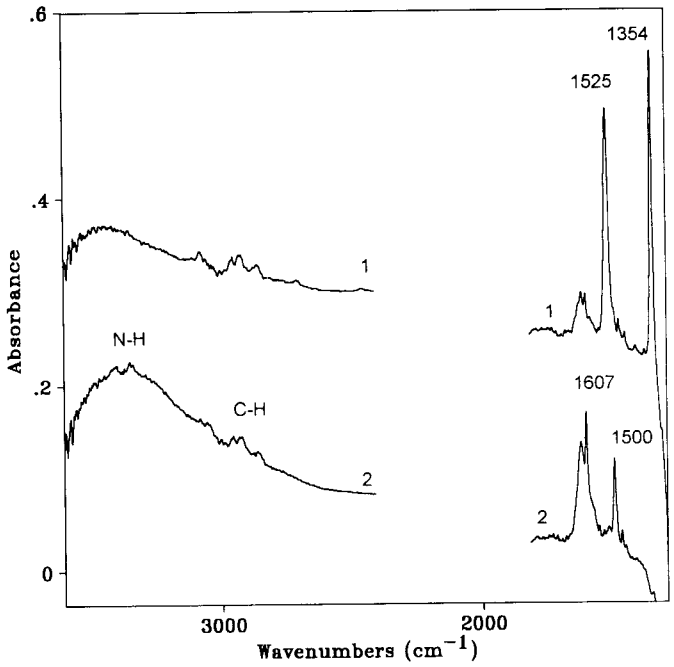

FIG. 9. Absorbance IR spectra produced by interaction of nitrobenzene on sample 3: curve 1, 2 Torr of nitrobenzene; curve 2, spectrum run after 10 min contact with H_2 (10 Torr).

bands due to the N–H stretching and an increase of the hydroxyl absorption are observed in the high-frequency region (Fig. 9, curve 2).

Activity

The hydrogenation experiments have been performed in a large excess of hydrogen so that the reactor pressure can be assumed as constant. The product distribution during the reaction is similar for both the monometallic and the bimetallic catalysts and a typical reaction profile obtained on a Pd–Fe/SiO_2 catalyst (sample 6) is shown in Fig. 10. As it appears the first stage of the reaction (i.e., the consumption of 2,4-DNT) occurs rather quickly and displays a typical zero-order dependence on the reactant concentration. The two half-hydrogenated products 2-nitro-4-aminotoluene and 2-amino-4-nitrotoluene (hereafter 2N-4AT and 2A-4NT, respectively) begin to form immediately and reach a maximum concentration when 2,4-DNT is completely consumed. As to the final product 2,4-TDA, its formation displays a clear induction period until all 2,4-DNT has been consumed and its rate of formation undergoes a sharp increase only when the two half-hydrogenated intermediates reach the maximum concentration. Since the two stages are well separated, when analyzing the disappearance of the two intermediate aminonitrotoluenes, a zero-order dependence on their total concentration can again be observed. All these features

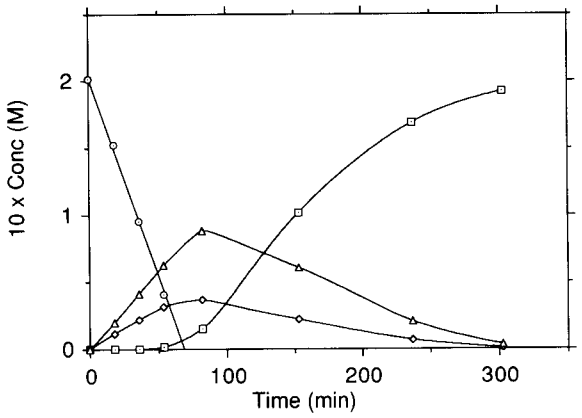

FIG. 10. A typical reaction profile for the hydrogenation of 2,4-DNT (sample 6 as catalyst). Circles: 2,4-DNT; squares: 2,4-TDA; triangles: 2N-4AT; diamonds: 2A-4NT.

are typical and are in agreement with previously reported examples of the hydrogenation of 2,4-DNT, which is known to be a mechanistically very complex reaction (45).

The rate constants that can be calculated from the individual plots are reported in Table 4. If we consider the first stage, the order of reaction with respect to 2,4-DNT implies that the active sites of the catalysts will have to be completely saturated, even at low 2,4-DNT concentrations, under the reaction conditions employed. Since the IR analysis carried out for nitrobenzene adsorption indicates that this substrate is adsorbed on the support, at least macroscopically, it seems reasonable to assume the same type of chemisorption for 2,4-DNT also. On the other hand, hydrogen is clearly activated on the metal phase; therefore, the simple assumption of the hydrogen transfer as the rate-determining step of the reaction seems to be the most straightforward interpretation of the observed kinetic dependence. Under this hypothesis, the mutual interaction between the chemisorbed species to give products would occur only at the relatively few interface sites between metal particles and support.

TABLE 4

Zero-Order Rate Constants for the First Stage (k_1) and the Second Stage (k_2) of the Hydrogenation of 2,4-DNT

Catalyst no.	Fe/Pd (atomic)	$k_1 \times 10^5$ ($M\ s^{-1}$)	$k_2 \times 10^5$ ($M\ s^{-1}$)
1	0.0	4.4	1.2
2	0.49	7.0	1.4
3	0.73	7.5	1.4
4	0.97	7.8	1.6
5	1.55	7.2	1.5
6	2.13	6.4	1.1
7	4.17	6.17	1.2

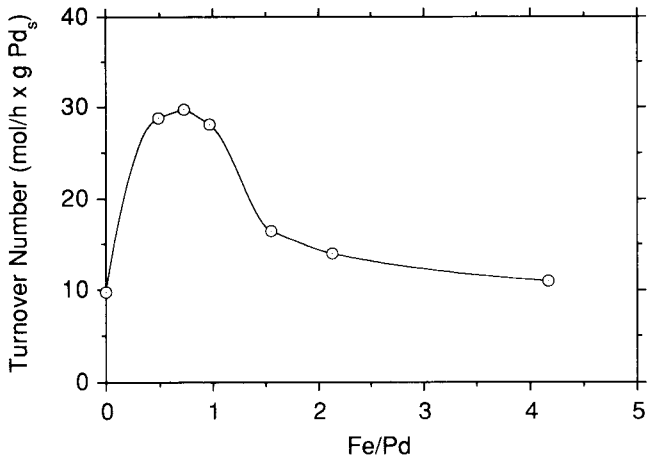

FIG. 11. Turnover data (mol · h^{-1} · g^{-1} Pd_s) for the disappearance of 2,4-DNT (first stage of the reaction) vs the Fe/Pd atomic ratio of the individual catalysts.

In previous work (14, 46) on the hydrogenation of nitrobenzene and 2,4-DNT on a variety of Pd/SiO_2 catalysts a similar kinetic behaviour was observed and it was found that the reaction was favoured by an increase of the metal particle size, leading to the suggestion that the reaction was controlled by the ability of the metal to spill the β-hydrogen stored in the bulk of the metal particle. In view of the fact that the substrate is chemisorbed on the support, this would suggest that hydrogen transfer occurs from the metal to the support where the substrate is hydrogenated.

Further support to this view can be obtained by analyzing the behaviour of unsupported palladium. A Pd black (particle size ~20 nm) was tested in the hydrogenation of 2,4-DNT under the experimental conditions of Table 4 and Fig. 10. No catalytic activity was observed, thereby emphasizing the role of the support in promoting the reaction.

Coming to the present catalysts, an analysis of the effect of the iron content can be better understood if the data of Table 4 are normalized to the Pd-exposed surface sites measured by hydrogen chemisorption and plotted as a function of the Fe/Pd ratio (Fig. 11). As can be seen an increase of the activity with respect to Pd/SiO_2 is observed for all catalysts, this being particularly evident in the samples with Fe/Pd < 1 that are characterized by relatively large metallic particles showing a disordered microstructure. Although the dispersion within the Fe–Pd series cannot be measured quantitatively for the reasons previously mentioned, the general indications of the XRPD and HRTEM analysis and the H_2 chemisorption data seem to be that an increase of dispersion of the Fe–Pd alloy is associated with the increase of the Fe content of the catalysts. On the other hand, as shown by the TPR profiles (Fig. 1), a modest amount of β-hydride seems to be present only in samples 2 and 3. Therefore, the almost identical specific activity displayed by the three most active catalysts seems to be independent of both the metal particle size and the possible β-hydride formation.

This discrepancy between Pd and Pd–Fe catalysts seems to suggest that a different mechanism is operative in the latter case. A possible mechanistic view of the present catalytic system is shown in Fig. 12a. It is suggested that 2,4-DNT chemisorbs on SiO_2 with one nitro group, while the second nitro group dangles from the surface and, at the metal–support interface, can come in contact with the alloy particles. This will lead to hydrogen transfer, probably via a cooperative effect of Fe in $-NO_2$ activation, a pathway that is not accessible to Pd alone. An additional factor making hydrogen transfer easier is the high reticular disorder and the presence of stacks and dislocations at the alloy surface evidenced by HRTEM (Fig. 5a) that would result in more reactive surface Pd sites. Studies on single-crystal surfaces showed that stepped surfaces are more active than flat ones (47), while molecular beam studies of H_2/D_2 exchange showed a dissociation probability on these surfaces 7–10 times higher than that on flat planes (48). Moreover, as indicated by the disappearance of the band at 1983 cm^{-1} in the CO absorption spectra, the iron causes the complete depletion of a type of adsorption site usually present at Pd surfaces, where CO is adsorbed in a bridged, "compressed" form.

However, the XRPD analysis suggests also that, as the Fe/Pd ratio increases, the alloy surface could become covered with increasing amounts of different (catalytically inactive) Fe species. This does not affect the H_2 chemi-

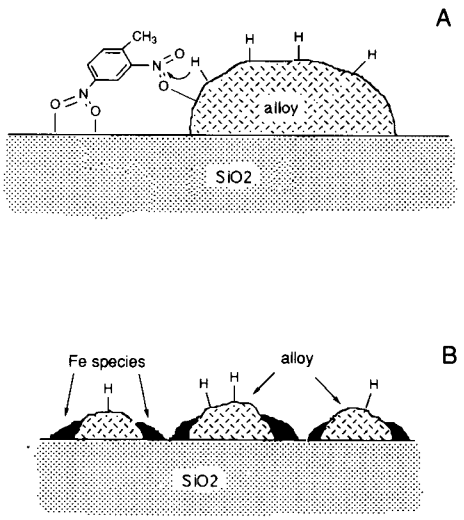

FIG. 12. (A) A schematic view of the hydrogen transfer step on 2,4-DNT at the interface between alloy particles and support; (B) a schematic view of the catalyst surface at high Fe content.

sorption properties, but does affect the catalytic activity, suggesting that this "excess' Fe is localized mainly at the borderline between alloy particles and support (Fig. 12b). This would lead to an overall decrease of the catalytic activity and explain the shape of the curve reported in Fig. 11.

As to the second stage of the reaction, the zero-order rate constants reported in Table 4 seem to parallel the same trend (although less pronounced) observed for the first stage, suggesting a similar interpretation.

CONCLUSIONS

In trying to summarize a few general conclusions from the present work, it can be said that the addition of Fe to Pd/SiO_2 catalysts results in the formation of a Pd–Fe alloy, the composition of which has been shown with XRPD analysis for samples with a low total Fe content. Alloy formation is also consistent with the results of other physicochemical characterizations, namely IR, HRTEM, TPR, and chemisorption.

The increase of the overall amount of Fe in the catalysts results in the increase of the alloy particle dispersion and the parallel formation of other Fe species mainly located at the interface between alloy particle and support. Moreover, the IR analysis suggests the presence of partially oxidized Fe atoms at the surface of the alloy.

Another important IR indication is that nitrobenzene used as a probe chemisorbs mainly on the SiO_2 support instead of the metal surface.

Finally, all bimetallic catalysts are more active than the one containing only Pd and it is suggested that Fe in the alloy cooperates in the hydrogen transfer step, probably through an interaction with the nitro group.

ACKNOWLEDGMENTS

Financial support from MURST and CNR is gratefully acknowledged. Thanks are expressed to Miss T. Fantinel (University of Venice) for skillful technical assistance.

REFERENCES

1. Jacobson, R. L., U.S. Patent No. 4,059,645 (1977).
2. Sinfelt, J. H., U.S. Patent No. 3,953,368 (1976).
3. Carter, J. L., and Barnett, A. E., U.S. Patent No. 4,251,394 (1981).
4. Carter, J. L., Barnett, A. E., and Sinfelt, J. H., U.S. Patent No. 4,263,173 (1981).
5. Sachtler, W. M. H., *Catal. Rev.-Sci. Eng.* **14,** 193 (1976).
6. Ponec, V., *Adv. Catal.* **32,** 143 (1983).
7. Boitiaux, J. P., Csyns, J., Derrien, M., and Léger, G., *Hydrocarbon Process.* **3,** 51 (1985).
8. Mallat, T., Petrò, J., Szabò, S., and Sztatisz, J., *React. Kinet. Catal. Lett.* **29,** 353 (1985).
9. Mallat, T., and Petró, *Appl. Catal.* **4,** 257 (1982).
10. Galvagno, S., Donato, A., Neri, G., Pietropaolo, R., and Poltarzewki, Z., *J. Mol. Catal.* **42,** 379 (1987).
11. Graham, P. D., and Spiegler, L., U.S. Patent No. 2,823,235 (1958).
12. Seagraves, R. L., U.K. Patent 2,024,643 (1980).
13. Strätz, A. M., *in* "Catalysis of Organic Reactions" (J. R. Kosak, Ed.), p. 335. Dekker, New York, 1984.
14. Benedetti, A., Fagherazzi, C., Pinna, F., Rampazzo, G., Selva, M., and Strukul, G., *Catal. Lett.* **10,** 215 (1991).
15. Dall'Agnol, C., Gervasini, A., Morazzoni, F., Pinna, F., Strukul, G., and Zanderighi, L., *J. Catal.* **96,** 106 (1985).
16. Fagherazzi, G., Benedetti, A., Martorana, A., Giuliano, S., Duca, D., and Deganello, G., *Catal. Lett.* **6,** 263 (1990).
17. Enzo, S., Benedetti, A., and Polizzi, S., *Z. Kristallogr.* **170,** 275 (1985).
18. Nandi, R. K., Kuo, H. K., Schlossberg, W., Wissler, G., Cohen, J. B., and Crist Jr., B., *J. Appl. Crystallogr.* **17,** 22 (1984).
19. Warren, B. E., and Averbach, B. L., *J. Appl. Phys.* **21,** 1059 (1950).
20. Joyal, C. L., and Butt, J. B., *J. Chem. Soc., Faraday trans. 1* **83,** 2757 (1987).
21. Lietz, G., Nimz, M., Völter, J., Lázár, K., and Guczi, L., *Appl. Catal.* **45,** 71 (1988).
22. Hurst, N. W., Gentry, S. J., and Jones, A., *Catal. Rev.-Sci. Eng.* **24,** 233 (1982).
23. Lieske, H., Lietz, G., Hanke, W., and Völter, J., *Z. Anorg. Allg. Chem.* **527,** 135 (1985).
24. Unmuth, E. E., Schwartz, L. H., and Butt, J. B., *J. Catal.* **87,** 8 (1983).
25. Garten, R. L., and Ollis, D. T., *J. Catal.* **35,** 232 (1974).
26. Garten, R. L., *J. Catal.* **43,** 18 (1976).
27. Homeyer, S. T., Sheu, L. L., Zhang, Z., Sachtler, W. M. H., Balse, V. R., Dumesic, J. A., *Appl. Catal.* **64,** 225 (1990).
28. Guerrero Ruiz, A., Sepúlveda-Escribano A., and Rodríguez-Ramos, I., *Appl. Catal.* **81,** 81 (1992).
29. Richard, D., Ockelford, J., Giroir-Fendler, A., and Gallezot, P., *Catal. Lett.* **3,** 53 (1989).
30. Guczi, L., *Catal. Rev.-Sci. Eng.* **23,** 329 (1981).
31. Wielers, A. F. H., Kock, A. J. H. M., Hop, C. E. C. A., Geus, J. W., and van Der Kraan, A. M., *J. Catal.* **117,** 1 (1989).
32. Raub, E., Beeskow, H., and Loebich, O., *Z. Metallkd.* **54,** 549 (1963).
33. Niemantsverdriet, J. W., van Kaam, J. A. C., Flipse, C. F. J., and van der Kraan, A. M., *J. Catal.* **96,** 58 (1985).
34. Nimz, M., Lietz, G., Völter, J., Lazar, K., and Guczi, L., *Catal. Lett.* **1,** 93 (1988).
35. Bartholomew, C. H., and Boudart, M., *J. Catal.* **29,** 278 (1973).
36. Bradshaw, A., and Hoffman, F. M., *Surf. Sci.* **72,** 513 (1978).
37. Shen, L. L., Karpinski, Z., and Sachtler, W. M. H., *J. Phys. Chem.* **93,** 4890 (1989).
38. Udovic, T. J., and Dumesic, J. A., *J. Catal.* **89,** 314 (1984).
39. Sona-Noto, Y., and Sachtler, W. M. H., *J. Catal.* **34,** 162 (1987).
40. Rodriguez, J. A., and Goodman, D. W., *J. Phys. Chem.* **95,** 4196 (1991).
41. Yuen, S., Chen, Y., Kubsh, J. E., Dumesic, J. A., Topsoe, N., and Topsoe, H., *J. Phys. Chem.* **86,** 3022 (1982).
42. Cocke, D. L., Hess, T. R., Mebrahnu, T., Mencer, D. E., Jr., and Naugle, D. G., *Solid State Ionics* **43,** 119 (1990).
43. Koutstaal, C. A., Angevaare, P. A. J., Grostendorst, E. J., and Ponec, V., *J. Catal.* **141,** 82 (1993).
44. Kline, C. H., Jr., and Torkevich, J., *J. Chem. Phys.* **12,** 300 (1944).
45. Janssèn, H. J., Kruithof, A. J., Steghuis, G. J., and Westerterp, K. R., *Ind. Eng. Chem. Res.* **29,** 754 (1990).
46. Selva, M., Dr. thesis, University of Venice, Venice, Italy, 1989.
47. Iang, P., Joyner, P. W. and Somorjai, G. A., *Surf. Sci.* **30,** 454 (1972).
48. Salmeron, M., Gale, R. J., and Somorjai, G. A., *J. Chem. Phys.* **67,** 5324 (1977).